Analysis of grid imprinting on geodesic spherical icosahedral grids

Pedro S. Peixoto, Saulo R. M. Barros*

Instituto de Matemática e Estatística - Universidade de São Paulo, R. do Matão 1010, 05508-090 São Paulo, Brazil

Abstract

Numerical grid imprinting errors have often been observed in global atmospheric models on icosahedral grids. In this paper we analyse the sources of grid imprinting error related to the usual finite volume discretization of the divergence operator. We introduce the concept of alignment of computational cells, and establish that convergence of second order is attained on aligned cells. Moreover, we present strong evidence that grid imprinting errors are caused by the slow convergence on badly aligned cells. The analysis presented is not restricted to icosahedral grids, being valid for any geodesic spherical grid.

Keywords: Icosahedral grid, geodesic grid, grid imprinting, grid alignment, alignment index, divergence discretization, discretization error

1. Introduction

Spherical geodesic grids, i.e. spherical grids whose cell edges are geodesic arcs, like the cubed sphere [1] and icosahedral grids [2], have been adopted in the development of new global atmospheric models [3]. The icosahedral grid is the most homogeneous among the Platonic solid based grids, and was chosen by several groups as the basis for global meteorological modelling [4, 5, 6, 7, 8, 9, 10].

In spite of the many advances on numerical models for icosahedral grids, including an operational model [6] and results towards fully 3D non-hydrostatic models [8, 11], some grid related issues still remain to be better understood. One of them is the phenomenon of grid imprinting [12, 13], in which geometrical grid properties become visible in numerical solutions.

Grid imprinting is directly related to numerical discretization accuracy, although not yet fully explained. For example, the usual finite volume discretization of the divergence operator (used in [5], [7], [8], [9]), in which the divergence at a computational cell (usually a Voronoi cell) is estimated using the fluxes at the cell edge midpoints, produces error patterns where coarse grid structures are evident. Tomita et al [5] suggested that grid imprinting was related to regions of high gradients of area and distortion distributions. Although the

*Corresponding author. Tel.: +55 11 30916136; fax: +55 11 30916131.

Email addresses: pedrosp@ime.usp.br (Pedro S. Peixoto), saulo@ime.usp.br (Saulo R. M. Barros)

area and distortion distributions present some correlation to the grid error pattern, they do not explain the error sources.

The purpose of this paper is to analyse the sources of discretization errors related to grid imprinting. We introduce the concept of aligned grid cells and show that the usual discretization of the divergence achieves second order on aligned cells. In order to quantify how well a cell is aligned we define an alignment index. For this discretization, we present evidence of a very sharp agreement of grid imprinting with bad alignment of cells.

Attempts to make the icosahedral grid more homogeneous with respect to distortion distribution led to the development of the Spring Dynamics grid optimization [14]. Heikes and Randall [15] introduced an optimization of the icosahedral grid in order to ensure consistency of a discretization of the Laplacian operator. Another approach is to optimize the icosahedral grid to make it a centroidal Voronoi tessellation [16, 17]. Miura and Kimoto [18] studied grid quality properties of several optimizations for icosahedral grids, with none of them being clearly better than the others. Although the grid optimizations contribute to reduce discretization errors and attenuate grid imprinting, they do not eliminate it. We present examples with spring dynamics, with the optimized grids from [15] and with centroidal Voronoi grids showing that the usual discretization of the divergence still produces error patterns related to the grid, which are matched very well by the alignment index.

Our theoretical results have been derived for the usual finite volume discretization of the divergence operator. This discretization is convenient due to its locality and simplicitly, requiring low computational costs and being amenable to parallelization. Our results do not cover other discretizations, which make use of higher order integration methods at cell edges for instance, but they are not restricted to the divergence operator or to icosahedral grids. We indicate how to extend the analysis to discretizations of the rotational and Laplacian operator. We also show analytically the existence of vector fields, for which the usual discretization of the divergence on regular triangular grids is no more than first order accurate. The alignment index can be applied to any type of geodesic spherical grids, like the cubed sphere, kite grids and octahedral grids. None of them is composed only of well aligned cells [1]. Our results indicate that the lack of alignment of the cells in certain regions of the grids is responsible for the discretization errors which cause grid imprinting. Unfortunately, the results do not provide the means to find well aligned spherical geodesic grids. In fact, topological properties of the sphere may prevent the existence of perfectly aligned geodesic grids. For instance, Euler's theorem shows that a spherical grid composed only of hexagonal cells cannot exist.

On the other hand, we should point out that our results do not imply that other discretizations of the divergence operator will not lead to higher order truncation errors on non aligned cells. In fact, the alignment index could serve as measure of where to use a more expensive discretization in order, for example, to achieve second order in the whole grid.

The paper is structured as follows. We begin showing grid imprinting evidences and how it can effect meteorological models in section 2. In section 3 we carry on the analysis of

[1] We carried out tests on octahedral grids, verifying that also in this case grid imprinting is matched by the alignment index. However, we do not include the results in this paper.

the sources of grid imprinting, starting with the results for planar polygons, followed by the extension of the theory to spherical geodesic grids. In section 4 we present numerical results, providing several examples of grid imprinting in agreement with the theoretical results, also for optimized grids. Our concluding remarks are presented in section 5.

2. Grid imprinting evidence and error propagation

Discretization errors related to the characteristics of icosahedral grids have been observed in many models (see e.g. [5]). This phenomenon, and ways to mitigate it, are still an actual research subject (see [13]). We illustrate its appearance in the discretization of the divergence and its propagation to other variables in a simplified version of a global transport model.

Consider for example a rotational vector field on the sphere, given in Cartesian coordinates as

$$\vec{v}(x, y, z) = (-y, x, 0), \tag{1}$$

where (x, y, z) is such that $x^2 + y^2 + z^2 = 1$. This is a non divergent vector field and therefore the computed divergence agrees with the error due to the discretization. In figure 1 we show the discretized divergence, calculated using the fluxes at the cell edge midpoints (cf. equation (4)), and we can clearly observe the grid imprinting on a glevel 6 icosahedral grid (see section 4.2 for the grid construction). Coarser-grid patterns are highly evidenced in the discretization errors.

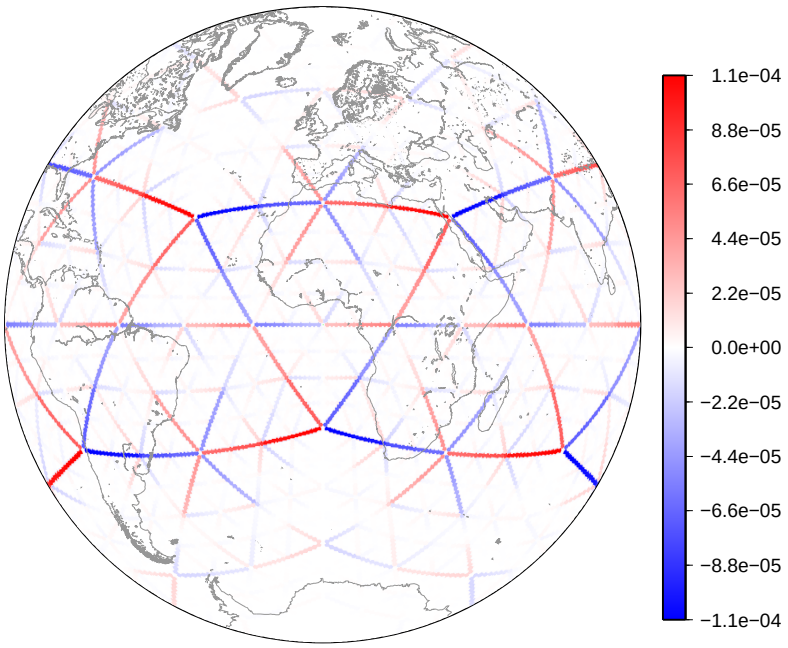

Figure 1: Error on divergence values for a rotation vector field on an icosahedral grid with glevel 6.

The repeated evaluation of the divergence with this kind of error can lead to strong background noise in the physical model solution. This can be seen, for instance, in the

density field of a global semi-Lagrangian transport model, composed by the mass continuity equation and a tracer conservation equation. We provide here only a brief description of the aspects relevant to the illustration of the propagation of grid imprinting. In advective form, the mass continuity equation is given by:

$$\frac{\partial \rho}{\partial t} + \mathbf{V}.\nabla\rho = \rho\nabla.\mathbf{V} \ , \tag{2}$$

where ρ is density and $\mathbf{V}$ the velocity field. As a simple case to illustrate the propagation of errors, we consider a deformational test case (suggested in [19] as test case number 4), which starts with a constant density field and a non divergent velocity field. Our semi-Lagrangian discretization of the mass equation has the form

$$\rho^{n+1} - \rho^{n}_{*} = \Delta t \ \ \frac{(\rho\nabla.\mathbf{V})^{n+1/2}_{*} + (\rho\nabla.\mathbf{V})^{n+1/2}}{2} \ \ , \tag{3}$$

where the superscripts refer to time instants, Δt is the time step and the subscript $*$ denotes the departure point of Lagrangian trajectories ending at the vertices of the triangulation. In this particular test case, the non-divergent wind is known and its exact expression is used at the cell edges where necessary. We have used an analytical third order approximation (given in [19]) for the determination of the departure points. A cubic hermite interpolation (as in [20]) was employed to obtain the density and divergence values at the departure point locations. The dominant error in the computations is related to the discretization of the divergence, which is of lower order as will be seen in this paper. The divergence discretization errors influence the density field, causing initially error patterns where grid imprinting is evident. With the time evolution we can observe the transport of these error patterns under the action of the deformational flow. The density field should remain constant, the error in its evaluation is displayed after 1, 4 and 120 time-steps in figure 2, showing the effects of grid imprinting. The sources of this kind of error are the subject of next section.

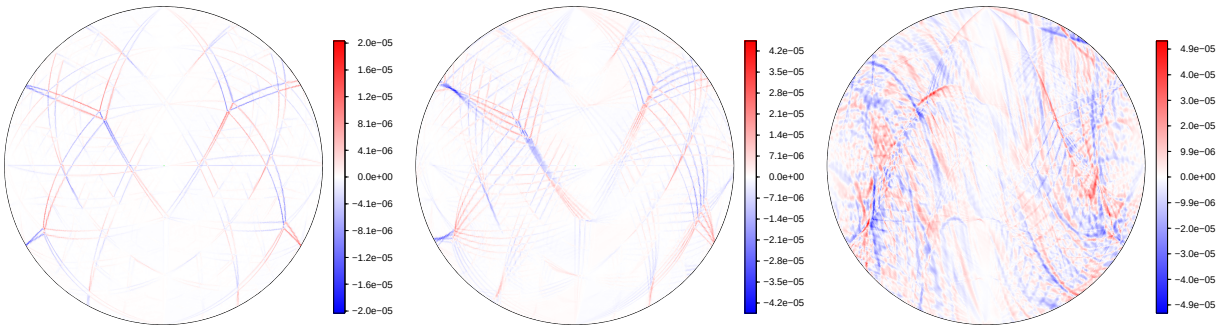

Figure 2: Errors in the density field after 1 (upper left), 4 (upper right) and 120 (bottom) time-steps of a global transport model on a glevel 6 icosahedral grid.

3. Sources of grid imprinting

In this section we analyse the source of the discretization errors of the divergence which lead to grid imprinting. We start by considering divergence approximations on planar poly-

gons, before proceeding to the spherical case.

3.1. Analysis of the discretization on a plane

Let Ω be a planar polygon with n sides. We denote by $|\Omega|$ its area and for each edge i let Q_i be its midpoint, l_i be the edge length and $\vec{n}_i$ the corresponding outer unit normal vector. Let $\vec{v}$ be a vector field on the plane. The usual approximation of the divergence at a point P_0 inside the polygon, based on Gauss divergence theorem, is given by:

$$\delta_d(P_0) = \frac{1}{|\Omega|} \sum_{i=1}^{n} \vec{v}(Q_i) \cdot \vec{n}_i \, l_i \, . \tag{4}$$

There are two sources of error in this discretization. The first is due to considering the divergence at a point as the average cell divergence, the second is due to the approximation of the line integral at an edge by the midpoint rule. It is simple to see that if P_0 is chosen as the center of mass of the polygon, then the mean divergence at the polygon is a second order approximation to the divergence at P_0. We denote by $d = \sup_{p,q\in\Omega} \|p - q\|$, the polygon's diameter. Using a Taylor expansion of the divergence $\delta = div(\vec{v})$ around P_0 we obtain

$$\frac{1}{|\Omega|} \int_\Omega \delta \, d\Omega = \delta(P_0) + \nabla\delta(P_0) \cdot \frac{1}{|\Omega|} \int_\Omega (P - P_0) \, d\Omega + \frac{1}{|\Omega|} \int_\Omega (P - P_0) \cdot (\nabla^2\delta(P_0)(P - P_0)) \, d\Omega + \cdots .$$

The second term of this expansion vanishes when P_0 is the center of mass of Ω. It results that

$$\left| \frac{1}{|\Omega|} \int_\Omega \delta \, d\Omega - \delta(P_0) \right| \leq C_a d^2, \tag{5}$$

where the constant C_a depends only on the Hessian of the divergence at P_0 ($\nabla^2\delta(P_0)$).

Using the above result we have the following error estimate for the discretization of the divergence at the center of mass P_0,

$$\begin{aligned} |\delta_d(P_0) - \delta(P_0)| &\leq \left| \delta_d(P_0) - \frac{1}{|\Omega|} \int_\Omega \delta \, d\Omega \right| + \left| \frac{1}{|\Omega|} \int_\Omega \delta \, d\Omega - \delta(P_0) \right| \\ &\leq \left| \delta_d(P_0) - \frac{1}{|\Omega|} \int_\Omega \delta \, d\Omega \right| + C_a d^2. \end{aligned} \tag{6}$$

We now analyse the errors due to the numerical integration by the midpoint rule. We parametrize the polygon edges as

$$\gamma_i(l) = l\vec{t}_i + Q_i, \quad l \in [-l_i/2, l_i/2] \tag{7}$$

where $\vec{t}_i$ is the unitary vector tangent to edge i in a counter-clockwise order (from P_i to P_{i+1}). From the divergence theorem we have

$$\begin{aligned}\frac{1}{|\Omega|}\int_\Omega \delta\, d\Omega &= \frac{1}{|\Omega|}\int_{\partial\Omega} \vec{v}\cdot\vec{n}\, d\partial\Omega = \frac{1}{|\Omega|}\sum_{i=1}^{n}\int_{\gamma_i} \vec{v}\cdot\vec{n}\, d\gamma_i \\ &= \frac{1}{|\Omega|}\sum_{i=1}^{n}\int_{-l_i/2}^{l_i/2} \vec{v}(\gamma_i(l))\cdot\vec{n}_i\, dl.\end{aligned}$$

Defining the normal velocity along the edge $w_i(l) = \vec{v}(\gamma_i(l))\cdot\vec{n}_i$ and expanding it around $l = 0$, we obtain after integrating

$$\int_{-l_i/2}^{l_i/2} \vec{v}(\gamma_i(l))\cdot\vec{n}_i dl = w_i(0)l_i + w_i''(0)\frac{l_i^3}{24} + O(l_i^5),$$

where the integrals of the odd terms in the polynomial expansion vanished. We observe that $w_i(0) = \vec{v}(Q_i)\cdot\vec{n}_i$ and that $w_i''(0)$ is the second derivative of the normal component of $\vec{v}$ in the tangential direction at point Q_i, that is $w_i''(0) = \vec{t}_i\cdot\nabla^2(\vec{v}(Q_i)\cdot\vec{n}_i)\vec{t}_i$, where $\nabla^2(\vec{v}(Q_i)\cdot\vec{n}_i)$ is the Hessian of the field $\vec{v}\cdot\vec{n}_i$ evaluated at Q_i. Altogether we get

$$\begin{aligned}\frac{1}{|\Omega|}\int_{\partial\Omega} \vec{v}\cdot\vec{n}\, d\partial\Omega = \frac{1}{|\Omega|}\sum_{i=1}^{n} \vec{v}(Q_i)\cdot\vec{n}_i\, l_i + \\ \frac{1}{|\Omega|}\sum_{i=1}^{n}\frac{l_i^3}{24}\vec{t}_i\cdot\nabla^2(\vec{v}(Q_i)\cdot\vec{n}_i)\vec{t}_i + \frac{1}{|\Omega|}\sum_{i=1}^{n} O(l_i^5). \quad (8)\end{aligned}$$

Assuming that exists a constant $\alpha > 0$ such $\alpha d^2 \le |\Omega|$, that is, Ω is not too distorted, then $1/|\Omega| \le 1/(\alpha d^2)$. Also using that $l_i \le d$, there is a constant C_b, depending only on the second order derivatives of the vector field and the geometry of the polygon, such that

$$\left|\frac{1}{|\Omega|}\int_{\partial\Omega} \vec{v}\cdot\vec{n}\, d\partial\Omega - \frac{1}{|\Omega|}\sum_{i=1}^{n}\vec{v}(Q_i)\cdot\vec{n}_i\, l_i,\right| \le C_b\frac{1}{d^2}d^3 \le C_b d. \quad (9)$$

This shows that in general, only a first order approximation can be expected with the discretization δ_d. However, if for instance the polygon is a square, the first order errors in the approximation of line integrals in opposite edges cancel each other, leading to a discretization of order two. In the following, we show this fact and establish more general conditions under which we can guarantee to achieve second order. We begin by introducing the concept of an aligned polygon.

Definition 1 (Planar aligned polygon)**.** *A polygon on a plane with an even number of vertices, given by $\{P_i\}_{i=1}^n$, is aligned if for each edge $e_i = \overline{P_iP_{i+1}}$ the corresponding opposite edge $e_{i+n/2} = \overline{P_{i+n/2}P_{i+n/2+1}}$ is parallel and has the same length as e_i (We assume a cyclic ordering of the vertices, that is, if $i > n$, then $P_i = P_{i-n}$).*

We now show that if a polygon is aligned, the discretization δ_d is an approximation of order two. For an aligned polygon n is even and from its definition it follows that $l_i = l_{i+\frac{n}{2}}$, $\vec{n}_i = -\vec{n}_{i+\frac{n}{2}}$ and $\vec{t}_i = -\vec{t}_{i+\frac{n}{2}}$ for $i = 1, .., \frac{n}{2}$. Employing these relations in (8) we obtain

$$\frac{1}{|\Omega|}\int_{\partial\Omega} \vec{v}\cdot\vec{n}\, d\partial\Omega = \frac{1}{|\Omega|}\sum_{i=1}^{n} \vec{v}(Q_i)\cdot\vec{n}_i\, l_i + \frac{1}{|\Omega|}\sum_{i=1}^{n/2} \frac{l_i^3}{24}\vec{t}_i\cdot\left(\nabla^2(\vec{v}(Q_i)\cdot\vec{n}_i) - \nabla^2(\vec{v}(Q_{i+n/2})\cdot\vec{n}_i)\right)\vec{t}_i + \frac{1}{|\Omega|}\sum_{i=1}^{n} O(l_i^5). \quad (10)$$

We observe that the terms of the Hessians $\nabla^2(\vec{v}(Q_i)\cdot\vec{n}_i)$ and $\nabla^2(\vec{v}(Q_{i+n/2})\cdot\vec{n}_i)$ differ only by $O(d)$, and since $l_i = O(d)$ for every i, we get from (10)

$$\frac{1}{|\Omega|}\int_{\partial\Omega} \vec{v}\cdot\vec{n}\, d\partial\Omega = \frac{1}{|\Omega|}\sum_{i=1}^{n} \vec{v}(Q_i)\cdot\vec{n}_i\, l_i + \frac{O(d^4)}{|\Omega|}. \quad (11)$$

As a consequence from (11) and (5) we have the following result.

Theorem 1. *Let $\vec{v}$ be a $\mathcal{C}^4$ vector field in R^2 and Ω be any aligned polygon in its domain, with diameter d and area $|\Omega|$ satisfying $\alpha d^2 \leq |\Omega| \leq d^2$, for some positive constant α. There exists a constant C_p, which is independent of the diameter d, such that*

$$\left| div(\vec{v})(P_0) - \frac{1}{|\Omega|}\sum_{i=1}^{n} \vec{v}(Q_i)\cdot\vec{n}_i\, l_i \right| \leq C_p d^2,$$

where P_0 is the center of mass of Ω.

3.2. Some remarks

In our analysis we assumed that the field $\vec{v}$ is exactly known at the locations where it is needed. In many models, this may not be the case, with interpolation or other form of reconstruction of the vector field being needed. From the analysis, we can deduce that the use of a third order approximation to the vector field $\vec{v}$ in the discretization of the divergence leads to a second order approximation on aligned cells, while a second order approximation to $\vec{v}$ may not be enough for that. A more extensive analysis of the interplay between different vector field reconstructions and the discretizations of the divergence and Laplacian operators on aligned cells is the object of undergoing work.

We point out, however, that even the use of the exact field values is not sufficient to guarantee second order on non aligned polygons. This is shown analitically in the following example for regular triangles and numerically through examples in section 4. We consider equilateral triangles with vertices located at $p_1 = l(-\frac{\sqrt{3}}{6}, \frac{1}{2})$, $p_2 = l(-\frac{\sqrt{3}}{6}, -\frac{1}{2})$ and $p_3 = l(\frac{\sqrt{3}}{3}, 0)$, whose centers of mass are at the origin and that have diameter $d = l > 0$. For a vector field given by

$$\vec{v} = \begin{bmatrix} u_0 + u_1 x + u_2 x^2 \\ 0 \end{bmatrix},$$

the actual value of the divergence at the origin is $\delta = u_1$, while the discretization will lead to $\delta_d = u_1 - l\frac{u_2}{4\sqrt{3}}$, with a first order error. Triangles are obviously non-aligned, since they have an odd number of sides. It is not difficult to provide a similar example for pentagons.

3.3. Analysis of the discretization on the sphere

Now we extend our results to the discretization of the horizontal divergence on the sphere

$$\delta_d(P_0) = \frac{1}{|\Omega|}\sum_{i=1}^{n} \vec{v}(Q_i)\cdot\vec{n}_i\, l_i, \tag{12}$$

where Ω is a spherical polygon, $|\Omega|$ is its geodesic area, Q_i are the edge midpoints, l_i the edge geodesic lengths and $\vec{n}_i$ the edge outer normal unit vectors. The point P_0 is the constrained mass *centroid* of Ω (see e.g. [17]). Observe that the center of mass P^* of a spherical polygon lies outside the polygon (inside the sphere). It is obtained as the point in R^3 such that $P^* = \int_\Omega P d\Omega$. The (constrained) mass centroid P_0 is the radial projection of the center of mass P^* onto the sphere ($P_0 = \frac{P^*}{||P^*||}$).

We will show that (12) is a second order discretization of the horizontal divergence when Ω is a spherical aligned polygon. In order to do that, as in the planar case, we first show that the average value of the divergence at the polygon is a second order approximation to the value of the divergence at the mass centroid (the details are presented in appendix B). Second, we need to show that the line integrals are also computed with a second order error. This part of the proof will be based on the results for planar polygons, considering the radial projection of Ω onto the tangent plane to the sphere at its centroid P_0. We first define an aligned polygon on the sphere:

Definition 2 (Spherical aligned polygon)**.** *A spherical polygon with an even number of edges is aligned if its radial projection onto the plane tangent to the sphere at its centroid is a planar aligned polygon.*

3.3.1. Radial projection of a polygon

We adopt Cartesian coordinates with the origin located at the center of the unit sphere, and with no loss of generality, we assume the north-pole to be located at the mass centroid $P_0 = (0, 0, 1)$ of the spherical polygon Ω. The geodesic edge joining vertices P_i and P_{i+1} of Ω will be named γ_i (in counter clockwise order), Q_i will be its midpoint. Its length will be $l_i = \arccos\langle P_{i+1}, P_i\rangle$ and $h_i = \arccos\langle P_i, P_0\rangle$ is the distance from P_i to P_0. These quantities are represented on figure 3. We also define:

- $h = \max_{i=1,\dots,n} h_i$ (the polygon radius),
- $l = \max_{i=1,\dots,n} l_i$ (the polygon maximum edge length),
- $d = \sup_{p,q\in\Omega} \arccos(\langle p, q\rangle)$ (the polygon diameter).

The radial projection of Ω onto the plane Γ, tangent to the sphere at P_0, will define a planar polygon Ω' in Γ. We observe that a point P on the sphere is projected at the intersection of the tangent plane with the straight line which joins P with the center of the sphere. We employ this projection only for points on the northern hemisphere, since we have placed P_0 at the north pole. We assume that Ω is entirely contained in this hemisphere. To each of the spherical polygon points, lengths and other quantities, there will be a corresponding one in the projected polygon, which we will denote with the addition of the symbol prime ($'$), as for example shown in figure 3, where the vertices P_i' are the respective projections of P_i, etc. Observe that for P on the sphere its projection is given by

$$P' = \frac{P}{\langle P, P_0 \rangle}, \tag{13}$$

and conversely, $P = \frac{P'}{\|P'\|}$.

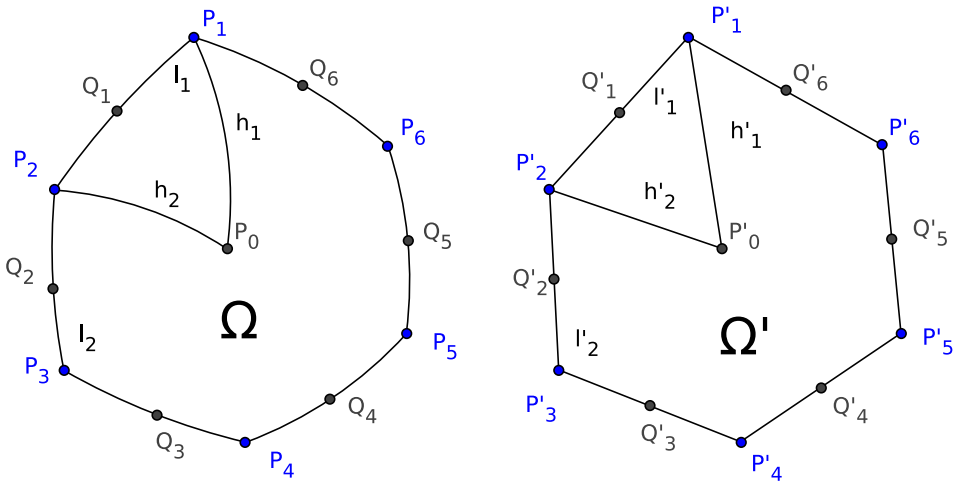

Figure 3: Indexation for the spherical polygon (on the left) and the projected planar polygon (on the right).

In appendix A we establish the following relations between quantities of both polygons. We have that $d' = d + O(d^3)$, $h_i' = h_i + O(d^3)$, $l_i' = l_i + O(d^3)$ and $|\Omega'| = |\Omega| + O(d^4)$. We also show that on spherical aligned polygons, the opposite sides have the same lengths ($l_i = l_{i+\frac{n}{2}}$).

3.3.2. Vector Field Projection

We have defined how to locally project a spherical polygon, defining a corresponding planar polygon on the plane Γ tangent to the sphere at P_0. To be able to transfer the analysis to the plane, we still need to define how to lift a vector field on the spherical polygon to the tangent plane Γ. This projection will be defined such that the local fluxes across the borders of the polygons are preserved. For this, at a point P of the polygon we consider the plane Λ tangent to the sphere at P and its intersection with a plane Γ_P, parallel to Γ and containing P. These two planes Λ and Γ_P intercept at a straight line ζ (see figure

4 for a representation) and form an angle $\phi_p < \pi/2$ between them. The vector $\vec{v}'$ at the point P' will be obtained through the rotation of $\vec{v}$ around ζ by the angle ϕ_p. That is,

$$\vec{v}'(P') = R_P \vec{v}(P), \tag{14}$$

where R_P is a rotation matrix that, for the fixed plane Γ, depends only on the point P, but not on $\vec{v}$. We point out that this projection corresponds to an orthogonal projection of $\vec{v}$ onto Γ, followed by a restoration of its original magnitude. Since (R_p) varies smoothly with P, the projected field $\vec{v}'$ is as differentiable as $\vec{v}$.

We now show that fluxes across the borders are preserved. For Q being a point of the boundary of Ω and Q' it's radial projection onto Γ, let $f(Q) = \vec{v}(Q) \cdot \vec{n}_Q$ and $f'(Q') = \vec{v}'(Q') \cdot \vec{n}'_{Q'}$ be the normal fluxes at these edge points on the sphere and on the projected plane, respectively. Noticing that a rotation matrix is orthogonal (i.e. $(R_p)^t R_p = I$), we have

$$\begin{aligned} f'(Q') &= \vec{v}'(Q') \cdot \vec{n}'_{Q'} = (R_Q \vec{v}(Q))^t R_Q \vec{n}_Q \\ &= (\vec{v}(Q))^t (R_Q)^t R_Q \vec{n}_Q = \vec{v}(Q) \cdot \vec{n}_Q \\ &= f(Q). \end{aligned} \tag{15}$$

This property also implies that the horizontal divergence on the sphere at the point P_0 coincides with the divergence given by the planar vector field $\vec{v}'$ at the same point (see appendix C for details).

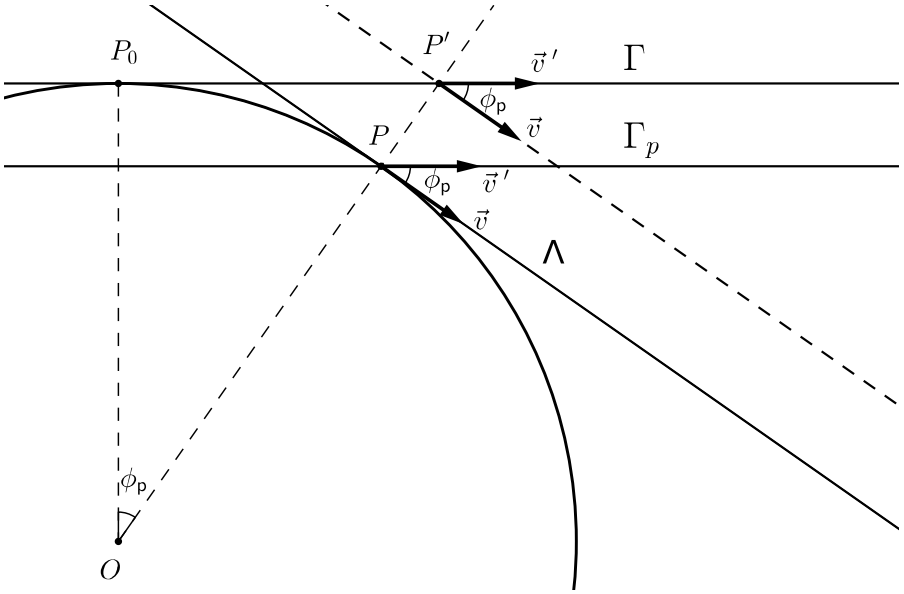

Figure 4: Elements involved in vector projection.

3.3.3. Convergence Analysis

Now we are ready to show that on aligned spherical polygons the usual discretization of the divergence operator δ_d is second order accurate, although only first order accuracy can be guaranteed for general spherical polygons. To estimate the error in the discretization of the divergence $\delta = \mathrm{div}(\vec{v})(P_0)$, we will add and subtract the discretization of the divergence of the projected field. We observe that $\mathrm{div}(\vec{v}')(P_0) = \mathrm{div}(\vec{v})(P_0)$ and since $P_0 = \bar{P} + O(d^2)$ (see appendix B), $\mathrm{div}(\vec{v}')(P_0) = \mathrm{div}(\vec{v}')(\bar{P}) + O(d^2)$, where $\bar{P}$ is the center of mass of the projected polygon. We then have

$$\begin{aligned}
&\left|\delta - \frac{1}{|\Omega|}\sum_{i=1}^{n} \vec{v}(Q_i)\cdot\vec{n}_i\, l_i\right| = \\
&\quad = \left|\delta - \frac{1}{|\Omega'|}\sum_{i=1}^{n} \vec{v}'(Q_i')\cdot\vec{n}_i'\, l_i' + \frac{1}{|\Omega'|}\sum_{i=1}^{n} \vec{v}'(Q_i')\cdot\vec{n}_i'\, l_i' - \frac{1}{|\Omega|}\sum_{i=1}^{n} \vec{v}(Q_i)\cdot\vec{n}_i\, l_i\right| \\
&\quad \le \left|\delta - \frac{1}{|\Omega'|}\sum_{i=1}^{n} \vec{v}'(Q_i')\cdot\vec{n}_i'\, l_i'\right| + \left|\frac{1}{|\Omega'|}\sum_{i=1}^{n} \vec{v}'(Q_i')\cdot\vec{n}_i'\, l_i' - \frac{1}{|\Omega|}\sum_{i=1}^{n} \vec{v}(Q_i)\cdot\vec{n}_i\, l_i\right| \\
&\quad = D + E.
\end{aligned}$$

The first term D can be estimated as follows:

$$\begin{aligned}
D &= \left|\delta - \frac{1}{|\Omega'|}\sum_{i=1}^{n} \vec{v}'(Q_i')\cdot\vec{n}_i'\, l_i'\right| \\
&\le \left|\delta - \mathrm{div}(\vec{v}')(\bar{P})\right| + \left|\mathrm{div}(\vec{v}')(\bar{P}) - \frac{1}{|\Omega'|}\sum_{i=1}^{n} \vec{v}'(Q_i')\cdot\vec{n}_i'\, l_i'\right| \le C_c d^2
\end{aligned}$$

where we used the results for planar polygons and that d and d' differ of $O(d^2)$. It remains to show that the second term E is of second order. It can be written as

$$\begin{aligned}
E &= \left|\frac{1}{|\Omega'|}\sum_{i=1}^{n} \vec{v}'(Q_i')\cdot\vec{n}_i'\, l_i' - \frac{1}{|\Omega|}\sum_{i=1}^{n} \vec{v}(Q_i)\cdot\vec{n}_i\, l_i\right| \\
&= \frac{1}{|\Omega|}\left|\frac{|\Omega|}{|\Omega'|}\sum_{i=1}^{n} \vec{v}'(Q_i')\cdot\vec{n}_i'\, l_i' - \sum_{i=1}^{n} \vec{v}'(Q_i')\cdot\vec{n}_i'\, l_i\right| \\
&= \frac{1}{|\Omega|}\left|\sum_{i=1}^{n} \vec{v}'(Q_i')\cdot\vec{n}_i'\cdot\left(\frac{|\Omega|}{|\Omega'|}l_i' - l_i\right)\right| \\
&= \frac{1}{|\Omega|}\left|\sum_{i=1}^{n/2} (\vec{v}'(Q_i') - \vec{v}'(Q_{i+n/2}'))\cdot\vec{n}_i'\cdot\left(\frac{|\Omega|}{|\Omega'|}l_i' - l_i\right)\right| \quad ,
\end{aligned}$$

where we used the equality between the fluxes across the spherical and the planar polygon borders. In the last equality we employed the fact that the lengths of opposite sides are the

same on planar, as well as on spherical, polygons and that the outer normal vectors of these sides are opposed to each other. We now recall that $|l_i - l'_i| = O(d^3)$, $|\Omega|/|\Omega'| = 1 + O(d^2)$ and that $l_i = O(d)$ to conclude that

$$E = \frac{O(d^3)}{|\Omega|} \left| \sum_{i=1}^{n/2} (\vec{v}'(Q'_i) - \vec{v}'(Q'_{i+n/2})) \cdot \vec{n}'_i \right|$$

Finally, we observe that $\vec{v}'(Q'_i) = \vec{v}'(P_0)+O(d)$ and $\vec{v}'(Q'_{i+n/2}) = \vec{v}'(P_0)+O(d)$. Therefore,

$$E = \frac{O(d^3)}{|\Omega|} \left| \sum_{i=1}^{n/2} O(d) \right| = O(d^2)$$

since $|\Omega| = O(d^2)$. This concludes the proof that we have a discretization error of order two for aligned spherical polygons. On the other hand, for non-aligned polygons only first order can be assured.

Theorem 2. *Let $\vec{v}$ be a $\mathcal{C}^4$ vector field on the sphere and Ω an aligned spherical polygon with n geodesic edges, diameter d and area $|\Omega|$ satisfying $\alpha d^2 \leq |\Omega| \leq d^2$, for some positive constant α. Then there is a constant C, which is independent of the diameter d, such that*

$$\left| div(\vec{v})(P_0) - \frac{1}{|\Omega|} \sum_{i=1}^{n} \vec{v}(Q_i) \cdot \vec{n}_i \, l_i \right| \leq C d^2,$$

where P_0 is the mass centroid of Ω.

3.3.4. Curl and Diffusion

The above results may be extended to the usual discretization of the curl and diffusion operators.

The rotational operator (*curl*) is usually discretized in a similar manner to the divergence,

$$\mathrm{curl}(\vec{v})(P_0) = \frac{1}{|\Omega|} \sum_{i=1}^{n} \vec{v}(Q_i) \cdot \vec{t}_i \, l_i,$$

where $\vec{t}_i$ are unit vectors tangent to the edges of the polygon. Replacing the normal vectors by the tangent vectors in our proofs, we will reach the same conclusions as for the divergence operator. That is, for an aligned spherical polygon the above discretization of the curl operator is second order if the tangential velocity is sufficiently accurate. On the other hand, no more than first order will be guaranteed globally.

The same conclusions will be valid for discretizations of the Laplacian, provided that the gradients of the field are computed with sufficient precision at the edge midpoints. In this case, the Laplacian will be obtained by employing the divergence discretization to the gradient of the field ($\Delta f = \nabla \cdot \nabla f$) and will be of second order on aligned spherical polygons.

4. Numerical Experiments

4.1. Icosahedral grid and measures of irregularity

A usual construction of the icosahedral grid starts by positioning the icosahedron with one vertex at each pole, with the result that the other 10 vertices will lie on latitudes $\pm \arctan(0.5)$. This basic positioning is show in figure 5 as the level 0 grid. Finer grids are obtained by adding nodes at the midpoints of the edges, recursively obtaining refined grids at different levels (glevels). The vertices of the triangles will be the grid nodes.

The icosahedral grid and it's refinements form Delaunay triangular grids, to which we can associate a Voronoi tessellation. These are shown in figure 5. The Voronoi cells are constructed by connecting the circumcenters of the triangles around a node (a more detailed description can be found in [18]). We are interested here in the case where the Voronoi polygons are used as computational cells. This is the most common approach in icosahedral based global models.

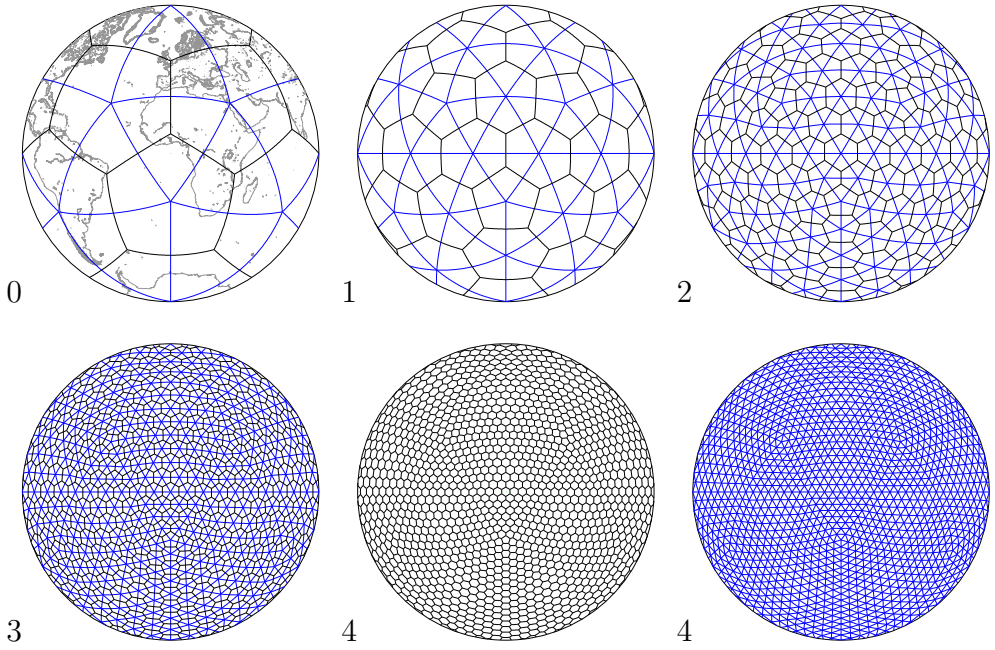

Figure 5: Delaunay triangulations and/or Voronoi cells are shown on different levels for icosahedral grids.

Several grid properties influence the quality of numerical approximations to differential operators. Among those, area uniformity and distortion of grid cells have been considered important measures of grid quality [5, 18]. As a measure for area uniformity we can employ the ratios between the cell areas and the maximum of these values. A measure of distortion for a given Voronoi cell Ω is given by the index

$$D(\Omega) = \frac{\sqrt{\frac{1}{n}\sum_{i=1}^{n}(l_i - \bar{l})^2}}{\bar{l}}, \tag{16}$$

where $\bar{l} = \sqrt{\frac{1}{n}\sum_{i=1}^{n} l_i^2}$, n is the number of edges of the cell Ω, l_i is the length of the ith edge. The area and distortion indexes for a glevel 6 icosahedral grid are shown in figure 6.

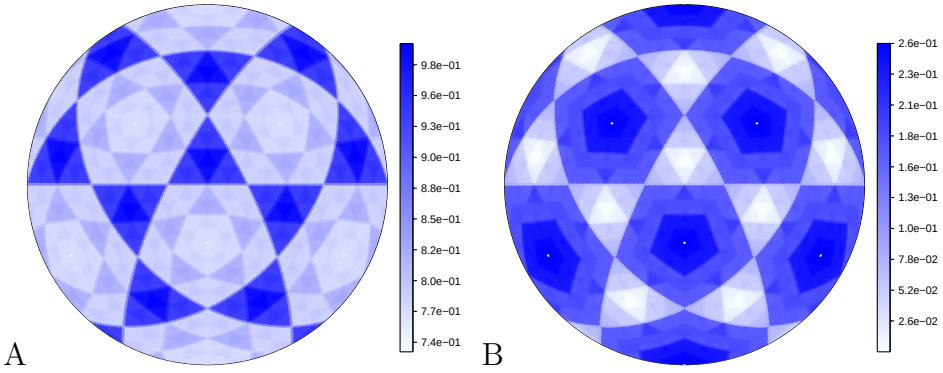

Figure 6: Distribution of area (A) and distortion (B) of Voronoi cells on a icosahedral grid glevel 6.

We have introduced the concept of aligned cells in section 3. We will now define a way of quantifying the alignment of cells, through an **alignment index**. This index will be defined for a polygonal cell Ω (spherical or not) with an even number of sides n as:

$$\Xi(\Omega) = \frac{1}{n\bar{d}} \sum_{i=1}^{n/2} |d_{i+1+n/2,i} - d_{i+n/2,i+1}| + |d_{i+1,i} - d_{i+n/2+1,i+n/2})|, \tag{17}$$

where $\bar{d} = \frac{1}{n}\sum_{i=1}^{n} d_{i,i+1}$, and $d_{i,j}$ is distance metric between polygon vertices P_i, $i = 1, ..., n$, and we identify $P_{n+1} = P_1$. For the planar case $d_{i,j} = d(P_i, P_j) = \|P_i - P_j\|$ is the Euclidian distance between points P_i and P_j, and on the sphere $d_{i,j} = d(P_i, P_j) = \arccos\langle P_i, P_j\rangle$ is the geodesic distance. The division by the mean edge length $\bar{d}$ provides normalization of the index. We have that $\Xi = 0$ if, and only if, Ω is aligned (using results from appendix A).

We employ this alignment index to quantify the degree of alignment of a cell. In figure 7 we observe that the maximum alignment index seems to atain a limit value on finer icosahedral grid levels. On the other hand, the average value of the alignment approaches zero, showing that aligned cells dominate more and more on finer grids.

It is quite remarkable how the pattern of the non-aligned cells matches the error distribution of the discretization error of the divergence operator (compare figure 1 with figure 8) in the example of the rotation presented in section 2. When compared to the other indicators (cf. figure 6), which also present some correlation with the error distribution, the alignment index leads to a much better match with the error pattern. Here, and in all the other numerical results in the paper, the exact and numerically evaluated divergence values are compared in the mass centroid of the cells.

4.2. Convergence experiments

We next consider the same test function used in [2] and [5]. This vector field is given in spherical coordinates as

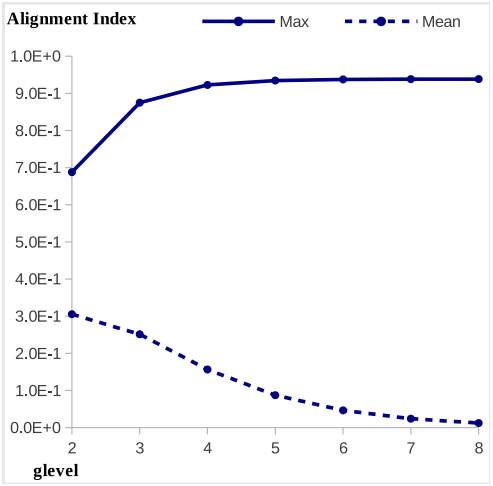

Figure 7: Maximum and average values of the alignment index of Voronoi cells on different icosahedral grid levels.

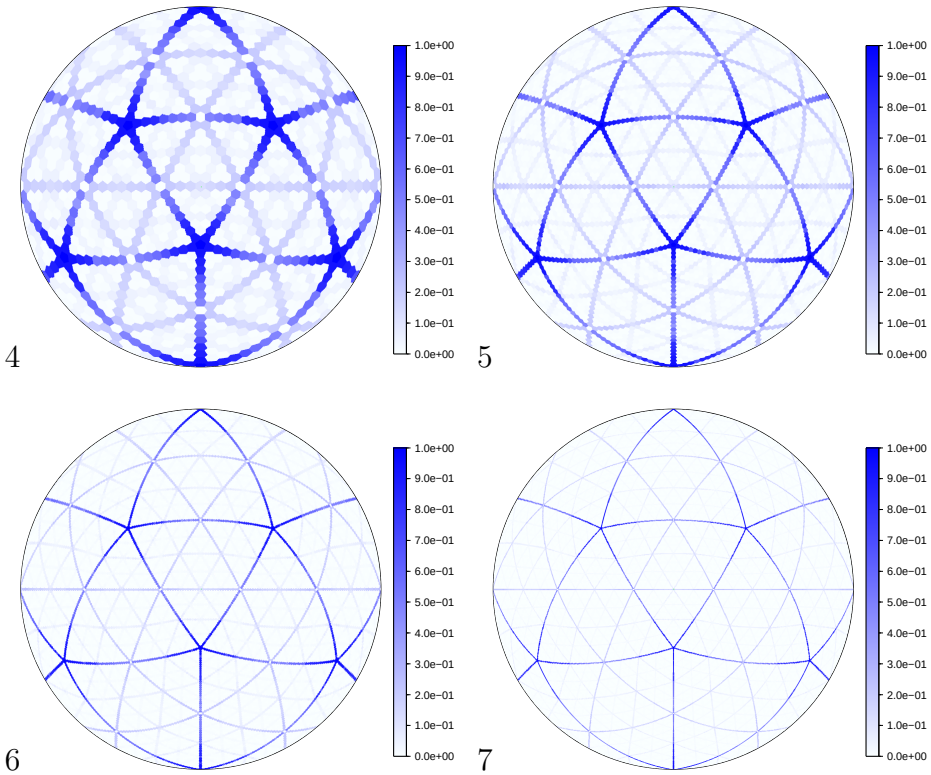

Figure 8: Distribution of the alignment index on different icosahedral grid levels.

$$u = -m\frac{\cos^4(n\theta)}{\cos(\theta)}\sin(\lambda)\sin(m\lambda) \quad (18)$$

$$v = -4n\cos^3(n\theta)\sin(n\theta)\sin(\lambda)\cos(m\lambda) \quad (19)$$

where $\lambda \in [-\pi, \pi]$ is the longitude, $\theta \in [-\pi/2, \pi/2]$ is the latitude, u and v are respectively the zonal and meridional vector field components, and m and n are integer constants.

4.3. Usual Icosahedral Grid

In figure 9 we show the error distribution of the estimates of the divergence on a glevel 6 ordinary icosahedral grid assuming $m = 1$ and $n = 1$. In general, the error follows the wave pattern of the divergence itself, being larger where the divergence is, as defined by the test case. However, there is a clear occurrence of grid imprinting in the error field. The largest errors occur where the alignment index is largest. Again there is a very good match between the index and the error patterns of grid imprinting. The distortion and area uniformity indicators are not so well correlated with grid imprinting.

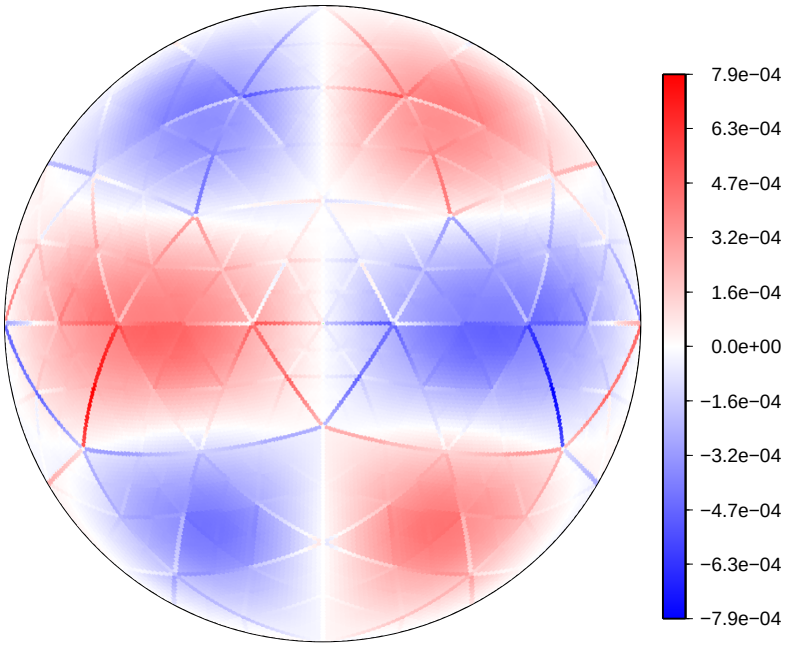

Figure 9: Error for the divergence estimates on an icosahedral grid with level 6, using $m = 1$, $n = 1$.

Next we show convergence results for successive levels of grid refinements. We observe that, in the maximum norm, the convergence of the discretization of the divergence is only of first order. We present evidences that the badly aligned cells cause the first order only convergence. As we have analysed, second order convergence should happen where the cells are well aligned. To verify this fact, we also computed the maximum norms only for better aligned cells (where $\Xi < 1/100$). The convergence results are shown in figure 10. The results

in quadratic norm are also shown and indicate that second order of convergence is achieved in this norm (observe that the proportional number of non-aligned cells - with $\Xi > 1/100$ - drops with the refinement of the grids). These results are compatible with those presented in [5]. We also point out that up to glevel 5, the maximum norm errors behave as if second order would be achieved. The reason for this is that in this test case the divergence in the regions close to the twelve (non-aligned) pentagons is close to zero. Large relative errors in these regions may be dominated by errors in the regions where the divergence is far from zero. With the refinement of the grids, the relatively larger errors become also the largest absolute values, since the convergence in these regions is only of first order.

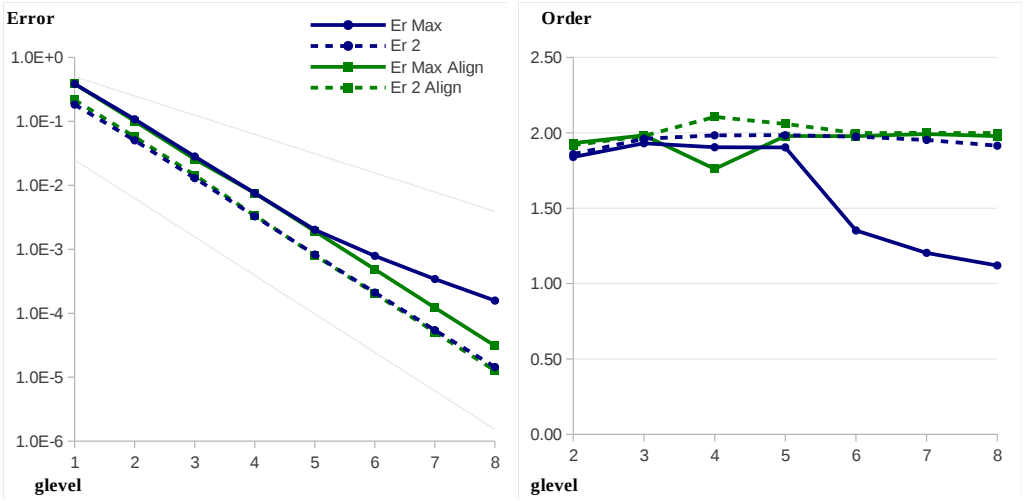

Figure 10: Convergence rates for the divergence discretization on the test vector field with $m = 1$ and $n = 1$. Error values are shown on the left and convergence orders estimates on the right, for each grid level. Errors in the maximum norm are shown in solid lines, while dashed lines are used for quadratic errors. Circles indicate global grid errors, while squares represent the errors restricted to regions of aligned cells. Thin dashed lines are reference lines for first and second order convergence.

4.4. Analysis on optimized grids

Several grid optimizations have been proposed for icosahedral grids. Among the most successful we mention the spring dynamics optimization (SPRG), the Heikes and Randall optimized grids (HR95) and the spherical centroidal Voronoi tessellation (SCVT). A review on the matter may be found in Miura [18]. We investigated the alignment properties of icosahedral grids optimized by these methods.

The spring dynamics optimization was proposed in the context of meteorological modelling in [5], with the main purpose to improve homogeneity of grid distortion. The original method solves an ordinary differential equations system to find the equilibrium state of the grid if the nodes where to be connected with virtual springs. We use the method proposed in Miura [18], that uses a relaxation method, in which iteratively each node is slightly moved in order to reduce distortion. We adopt the spring parameter of $\beta = 1.2$ recommended in [14],

and the relaxation parameter $\alpha = 0.09$. We stopped when differences in energy between consecutive iterations where less than $10E-9$.

The Heikes and Randall [15] grids were optimised so that the primal-dual cross-over points converge to the edge center with resolution. Their main objective was to reduce truncation erros in the discretization of the Laplacian.

On the usual icosahedral grid (see figure 5) the grid nodes do not necessarily coincide with the mass centroids of the Voronoi cells. On a spherical centroidal Voronoi tessellation the nodes are exactly the mass centroids of the Voronoi cells. To achieve this property, one can use Loyd's algorithm ([16]) departing from the usual icosahedral grid and iteratively moving the nodes to the mass centroids, within a given precision (we used $10E-10$).

In figure 11 we display the alignment index and the resulting errors in the discretizations of the divergence, with the same test case of the previous section, when employing the optimized grids. For the HR95 optimized grids the alignment pattern is similar to the non optimized icosahedral grids. However, we can observe a more substantial change in the configuration of the badly aligned cells of the SPRG and SCVT grids. They present a clustering around the grid pentagons in a star shaped form, assuming similar patterns on both optimized grids with slightly smaller values in the SCVT grid. We notice that grid imprinting does not disappear, but it follows the grid alignment pattern. The error again follows the wave pattern of the divergence itself but we observe the larger values on the non-aligned cells. SCVT leads to slightly smaller errors than spring dynamics, with somewhat larger errors being obtained with the HR95 grids. In comparison to the usual grid, the errors are reduced in all optimized grids.

On what concerns convergence, the qualitative behaviour on the optimized grids is unfortunately not much different from what is seen with the usual icosahedral grid. In figure 12 we present the maximum and quadratic norms of the discretization error on different grid refinement levels, together with the order of error reduction from level to level. As before, the quadratic errors present convergence of second order. The maximum errors, however, behave like second order in the first levels and then the first order of discretization becomes evident. The explanation is the same as before. In the non aligned cells the divergence errors are decaying only according to first order, while they decay faster on aligned cells. From a certain point on, the largest errors are on the non-aligned cells and they are reduced only by a factor of two on consecutive levels. To verify the second order behaviour on well aligned cells, we again computed the maximum error restricted to those cells. The results are also in figure 12 and show the second order convergence on aligned cells. In [5] it was claimed that second order convergence was achieved with spring dynamics, even with the maximum norm. Our results show that in fact only first order convergence in the maximum norm is guaranteed.

5. Concluding remarks

The importance of the geometric alignment of grid cells for the accuracy of numerical discretizations of differential operators has been shown. We were able to relate grid imprinting coming from the usual finite volume discretization of the divergence operator to a slower

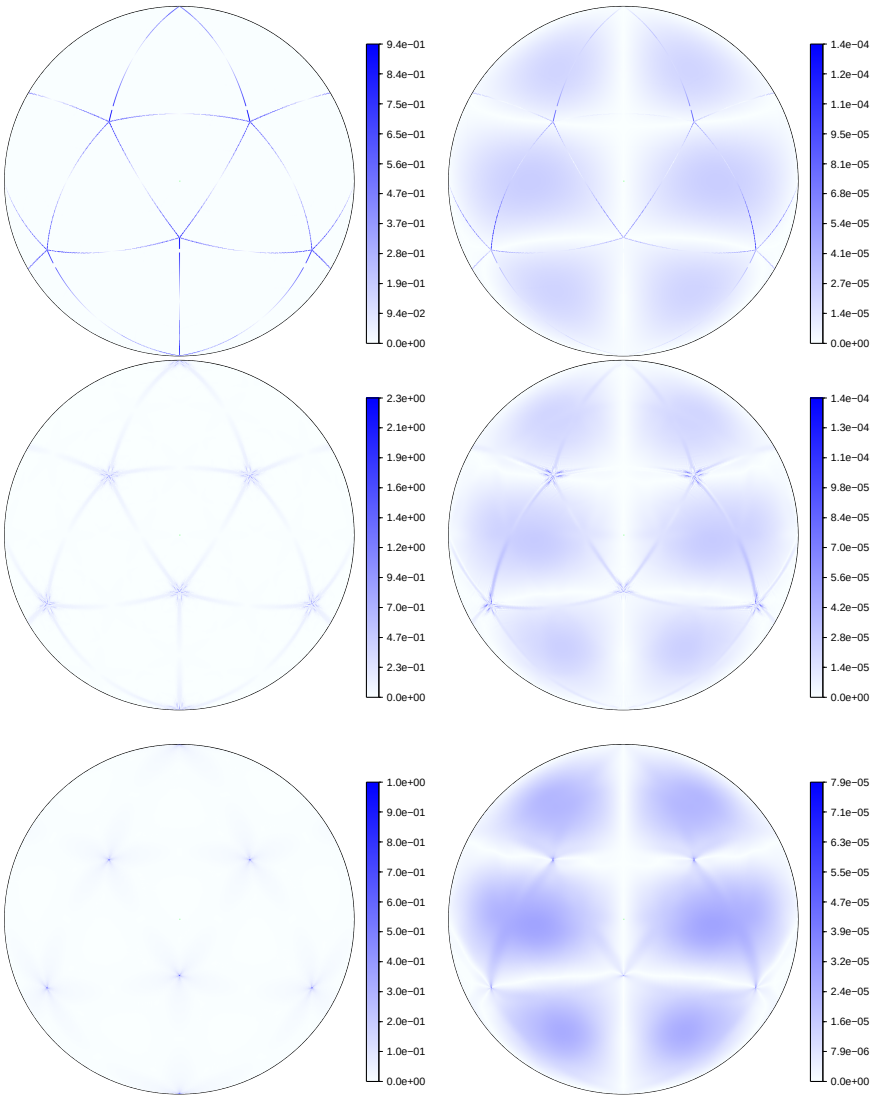

Figure 11: Alignment indexes (left) and divergence error (right) on test case $m = 1$ and $n = 1$ on optimized icosahedral grid g-level 8 with the HR95 optimized grids (top line), spring dynamics (middle line) and SCVT (bottom line).

convergence order on non-aligned grid cells. Second order of convergence is demonstrated for aligned grid cells when using this discretization. We have introduced an alignment index, which captures very well the phenomenon of grid imprinting. The theoretical results were shown first for planar polygons and then extended to the sphere. They are also applicable to the curl and Laplacian operators.

Even though we focused on geodesic icosahedral grids, the theory is valid to other geodesic grids, such as the kite-grids or cubed spheres, which also present grid imprinting [13]. A challenging question would be to construct a spherical geodesic grid containing only well

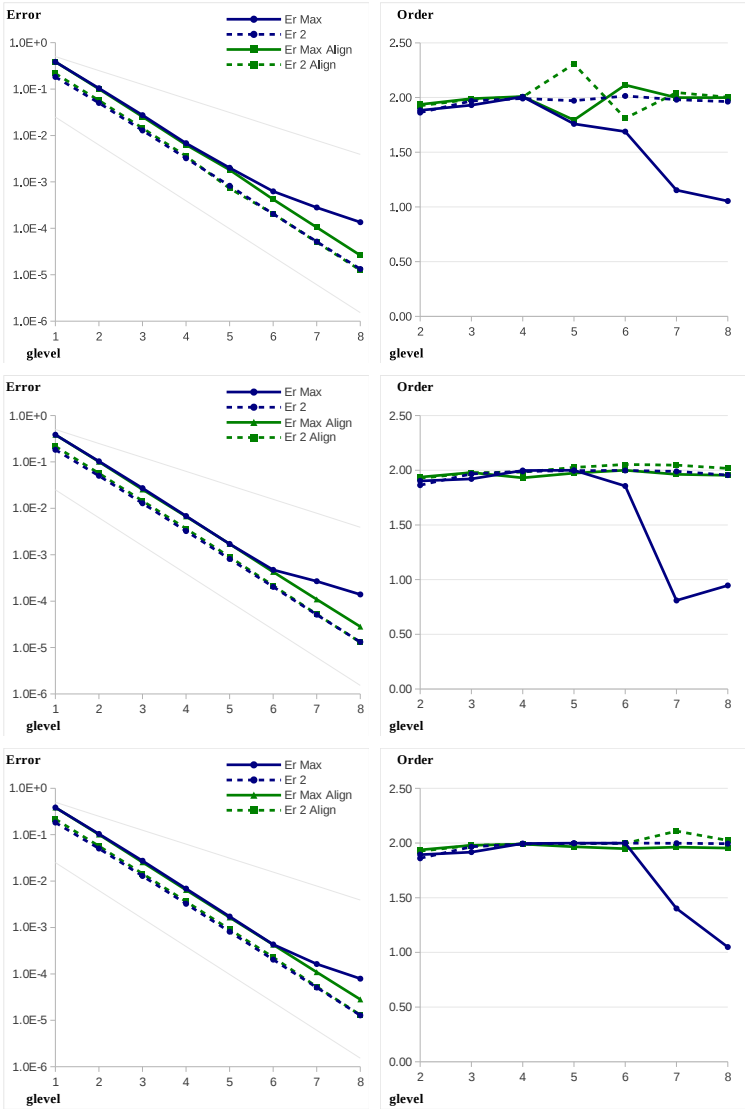

Figure 12: Same as figure 10 but now with HR95 (top line), spring dynamics (middle line) and SCVT (bottom line) optimizations.

aligned cells.

We notice that triangular grids fail to be aligned, as the cells have an odd number of edges. One can usually see a pattern of under/over shooting on neighbouring triangles [21]. Observe that two similar adjacent triangles may build an aligned quadrilateral when joined. Since the usual discretization of the divergence would be of second order on the aligned quadrilateral and only of first order on each individual triangle, we notice that these first order errors would have to compensate each other, explaining the error pattern.

In a completely aligned grid, all cells would need to have an even number of edges. Consequently, icosahedral grids, even with optimizations, cannot be completely aligned due to the 12 pentagons. An octahedral grid could, in principle, be a good candidate, since it can

be subdivided into hexagons and 6 rectangles. However, the hexagons near the rectangles are not well aligned, even if we apply the spring dynamics or centroidal Voronoi optimizations. On the cubed sphere, which also has only cells with an even number of edges, the cells near the vertices of the cube are far from being aligned.

From all this picture, it seems that the topology of the sphere may prevent the existence of a geodesic grid composed only of aligned cells. On the other hand, a regular latitude-longitude grid is such that a second order discretization of the divergence is achieved with the approach employed here. This is no contradiction, since the lat/lon grid is not geodesic. The use of non geodesic cell edges on icosahedral grids is a possibility to be investigated.

Another interesting approach can be the use of the alignment index as an indicator of where in the grid to employ a more sofisticated scheme to achieve second order. Since the fraction of badly aligned cells is rather small, this may provide an efficient way to obtain a globally second order method.

Acknowledgements We are grateful to Hillary Weller, to John Thuburn and to an anonymous referee for their comments and suggestions which helped to improve this paper. We thank Ross Heikes for kindly providing the HR95 grids to us. Financial support from Capes and CNPq is also acknowleged.

Appendix A. Comparison of magnitudes of a spherical polygon and of its planar projection

We provide here an analysis of the relative sizes of lengths and areas of a spherical polygon and its projection onto the plane tangent to the sphere at the constrained mass centroid P_0. First we observe that

$$h_i' = \tan(h_i) = h_i + O(h_i^3) = h_i + O(d^3) \tag{A.1}$$

and

$$\begin{aligned} l_i' &= \sqrt{\langle P_{i+1}' - P_i', P_{i+1}' - P_i' \rangle} \\ &= \sqrt{\left\langle \frac{P_{i+1}}{\langle P_{i+1}, P_0 \rangle} - \frac{P_i}{\langle P_i, P_0 \rangle}, \frac{P_{i+1}}{\langle P_{i+1}, P_0 \rangle} - \frac{P_i}{\langle P_i, P_0 \rangle} \right\rangle} \\ &= \sqrt{\frac{1}{\cos^2(h_i)} + \frac{1}{\cos^2(h_{i+1})} - 2\frac{\cos(l_i)}{\cos(h_{i+1})\cos(h_i)}}. \end{aligned} \tag{A.2}$$

Expanding l_i' with respect to l_i, h_i e h_{i+1} around zero of the 3 variables we have that

$$l_i' = l_i - \frac{1}{24} {l_i}^3 + \frac{1}{4} {h_{i+1}}^2 l_i + \frac{1}{4} {h_i}^2 l_i - \frac{1}{4} \frac{{h_i}^2 {h_{i+1}}^2}{l_i} + \frac{1}{8} \frac{{h_i}^4}{l_i} + \frac{1}{8} \frac{{h_{i+1}}^4}{l_i} \cdots = l_i + O(d^3) \quad .$$

The polygon diameter d' is given by

$$\begin{aligned} d' &= \sqrt{\langle P_j' - P_k', P_j' - P_k' \rangle} \\ &= \sqrt{\frac{1}{\cos^2(h_j)} + \frac{1}{\cos^2(h_k)} - 2\frac{\cos(l_{jk})}{\cos(h_j)\cos(h_k)}}, \end{aligned} \tag{A.3}$$

for some j and k and $l_{jk} = ||P_j - P_k|| = O(d)$. As for l'_i a Taylor expansion shows that $d' = d + O(d^3)$ and both diameters are of the same order.

We compare the areas of the polygons. Consider the transformation $\vec{\psi} : \Omega' \in \Gamma \to \Omega \in S^2$, where

$$\vec{\psi}(s,t) = \frac{1}{\sqrt{1+s^2+t^2}}(s,t,1).$$

Taking the norm of the cross product of the partial variations on each coordinate of Ψ, results in

$$\|\frac{\partial\,\vec{\psi}}{\partial s} \times \frac{\partial\,\vec{\psi}}{\partial t}\| = \frac{1}{(s^2+t^2+1)^{\frac{3}{2}}} = 1 - \frac{3}{2}\,s^2 - \frac{3}{2}\,t^2 + \frac{15}{8}\,t^4 + \frac{15}{4}\,t^2s^2 + \frac{15}{8}\,s^4 + \cdots .$$

Therefore

$$\begin{aligned} |\Omega| &= \int_\Omega d\Omega = \int_{\Omega'} \|\frac{\partial\,\vec{\psi}}{\partial s} \times \frac{\partial\,\vec{\psi}}{\partial t}\|\, d\Omega' \\ &= \int_{\Omega'} (1 - \frac{3}{2}\,s^2 - \frac{3}{2}\,t^2 + \frac{15}{8}\,t^4 + \frac{15}{4}\,t^2s^2 + \frac{15}{8}\,s^4 + \cdots)\, d\Omega' \\ &= |\Omega'| + \int_{\Omega'} (-\frac{3}{2}\,s^2 - \frac{3}{2}\,t^2 + \frac{15}{8}\,t^4 + \frac{15}{4}\,t^2s^2 + \frac{15}{8}\,s^4 + \cdots)\, d\Omega', \end{aligned}$$

and consequently

$$\frac{|\Omega|}{|\Omega'|} = 1 + O(d^2) \quad . \tag{A.4}$$

Now we can show that a spherical polygon Ω is aligned if, and only if, it has $\Xi(\Omega) = 0$. By the definition of spherical aligned polygon, all we need is to show that $\Xi(\Omega) = 0 \Leftrightarrow \Xi(\Omega') = 0$, which is equivalent to show that

$$l_i = l_{i+n/2} \Leftrightarrow l'_i = l'_{i+n/2},$$

and

$$d_{i,i+1+n/2} = d_{i+1,i+n/2} \Leftrightarrow d'_{i,i+1+n/2} = d'_{i+1,i+n/2},$$

for $i = 1, ..., n/2$, where $d_{j,k} = \arccos\langle P_j, P_k\rangle$ and $d'_{j,k} = \|P'_j - P'_k\|$. Using equation (A.1), we have that $h'_i = h'_{i+n/2} \Leftrightarrow h_i = h_{i+n/2}$. Now using this, and equation (A.2) we have the first part needed ($l'_i = l'_{i+n/2} \Leftrightarrow l_i = l_{i+n/2}$). For the rest, first notice that all geodesic arcs are projected as straight lines, and that if we assume $d_{i,i+1+n/2} = d_{i+1,i+n/2}$, and use that $h_i = h_{i+n/2}$, we have

$$
\begin{aligned}
d'_{i,i+n/2+1} &= \sqrt{\langle P'_{i+n/2+1} - P'_i, P'_{i+n/2+1} - P'_i \rangle} \\
&= \sqrt{\left\langle \frac{P_{i+n/2+1}}{\langle P_{i+n/2+1}, P_0\rangle} - \frac{P_i}{\langle P_i, P_0\rangle}, \frac{P_{i+n/2+1}}{\langle P_{i+n/2+1}, P_0\rangle} - \frac{P_i}{\langle P_i, P_0\rangle} \right\rangle} \\
&= \sqrt{\frac{1}{\cos\left(h_{i+n/2+1}\right)^2} + \frac{1}{\cos\left(h_i\right)^2} - 2\,\frac{\cos\left(d_{i,i+n/2+1}\right)}{\cos\left(h_{i+n/2+1}\right)\cos\left(h_i\right)}} \\
&= \sqrt{\frac{1}{\cos\left(h_i\right)^2} + \frac{1}{\cos\left(h_{i+n/2+1}\right)^2} - 2\,\frac{\cos\left(d_{i+1,i+n/2}\right)}{\cos\left(h_i\right)\cos\left(h_{i+n/2+1}\right)}} \\
&= \sqrt{\frac{1}{\cos\left(h_{i+n/2}\right)^2} + \frac{1}{\cos\left(h_{i+1}\right)^2} - 2\,\frac{\cos\left(d_{i+1,i+n/2}\right)}{\cos\left(h_{i+n/2}\right)\cos\left(h_{i+1}\right)}} \\
&= \sqrt{\langle P'_{i+n/2} - P'_{i+1}, P'_{i+n/2} - P'_{i+1} \rangle} \\
&= d'_{i+1,i+n/2}
\end{aligned}
$$

In the same way we can conclude that if $d'_{i,i+1+n/2} = d'_{i+1,i+n/2}$ then $d_{i,i+1+n/2} = d_{i+1,i+n/2}$.

Appendix B. Location of the centroid P_0 and value of the divergence

Locating the constrained mass centroid P_0 at the north pole, we have that the center of mass of Ω is necessarily of the form $P^* = (0, 0, z^*)$, with

$$
\begin{aligned}
z^* &= \frac{1}{|\Omega|}\int_\Omega z d\Omega = \frac{1}{|\Omega|}\int_{\Omega'} \frac{1}{\sqrt{1+s^2+t^2}} \| \frac{\partial\,\vec{\psi}}{\partial s} \times \frac{\partial\,\vec{\psi}}{\partial t} \|\, d\Omega' \\
&= \frac{1}{|\Omega|}\int_{\Omega'} (1 - 2\,s^2 - 2\,t^2 + 3\,t^4 + 6\,s^2t^2 + 3\,s^4 + \cdots)\, d\Omega' \\
&= \frac{|\Omega'|}{|\Omega|} + O(d^2) = 1 + O(d^2)
\end{aligned}
$$

and consequently $\|P^* - P_0\| \leq Cd^2$, for some constant C.

We now compare the location of P_0 with the center of mass $\bar{P}$ of Ω'. Both have z-

coordinate equal to 1. Let us evaluate the x-coordinate $\bar{x}$ of $\bar{P}$.

$$\begin{aligned}
0 &= \frac{1}{z^*|\Omega|}\int_\Omega x\, d\Omega \\
&= \frac{|\Omega'|}{z^*|\Omega|}\frac{1}{|\Omega'|}\int_{\Omega'} s\,\frac{1}{\sqrt{1+s^2+t^2}}\|\frac{\partial\vec{\psi}}{\partial s}\times\frac{\partial\vec{\psi}}{\partial t}\|\, d\Omega' \\
&= \frac{|\Omega'|}{z^*|\Omega|}\frac{1}{|\Omega'|}\int_{\Omega'} s\,(1-2\,s^2-2\,t^2+3\,t^4+6\,s^2t^2+3\,s^4+\cdots)\, d\Omega' \\
&= \frac{|\Omega'|}{z^*|\Omega|}\bar{x}-\frac{1}{z^*|\Omega|}\int_{\Omega'} s\,(2\,s^2+2\,t^2-3\,t^4-6\,s^2t^2-3\,s^4+\cdots)\, d\Omega' \\
&= \bar{x}+O(d^2)
\end{aligned}$$

Similarly, we have that $\bar{y}=O(d^2)$ and therefore $\|P^*-P_0\|=O(d^2)$.

We now compare the average value of the divergence in Ω with its value at the centroid P_0. Analogously to the planar case, given a smooth function $F:\mathbb{R}^3\to\mathbb{R}$ we have that

$$\frac{1}{|\Omega|}\int_\Omega F\, d\Omega \quad = \quad F(P^*) \quad + \quad \nabla F(P^*) \quad \cdot \quad \frac{1}{|\Omega|}\int_\Omega (P \quad - \quad P^*)\, d\Omega \quad + \quad O(d^2)$$

and since P^* is the center of mass of Ω the second term in the right hand side vanishes. Now, from the divergence field δ defined on the surface of the unit sphere, we can obtain the following smooth field, defined for $P\in\mathbb{R}^3, P\neq 0$, $F(P)=\delta(\frac{P}{\|P\|})$. Since F coincides with δ on Ω and $F(P^*)=\delta(P_0)$, we conclude that

$$\frac{1}{|\Omega|}\int_\Omega \delta\, d\Omega = \delta(P_0)+O(d^2)\ , \tag{B.1}$$

where the $O(d^2)$ term depends on the Hessian on a compact neighbourhood of Ω.

Appendix C. Vector projection preserves divergence

We show here that the vector projection preserves the divergence at the mass centroid P_0.

Let Θ be a circle cap on the sphere centered at P_0 with geodesic radius r. Its projection (Θ') is a circle region on Γ whose center is also P_0 and that has radius r', with $r'=\tan(r)$.

We can parametrize the border of Θ' as

$$\zeta'(t)=(r'\cos(t), r'\sin(t), 1), \tag{C.1}$$

where $t\in[0,2\pi]$ (remember that P_0 is at the north pole). With this parametrization we have that $\|\frac{d\zeta'(t)}{dt}\|=r'$. Now using the radial projection of points, this results in a natural parametrization for the border of Θ, a circle on the sphere,

$$\zeta(t)=\frac{\zeta'(t)}{\|\zeta'(t)\|}=\frac{1}{\sqrt{1+(r')^2}}(r'\cos(t), r'\sin(t), 1), \tag{C.2}$$

for which we have that

$$\|\frac{d\zeta(t)}{dt}\| = \frac{r'}{\sqrt{1+(r')^2}}. \tag{C.3}$$

Using both parametrizations we have

$$\begin{aligned}
\mathrm{div}(\vec{v})(P_0) &= \lim_{\Theta\to\{P_0\}} \int_{\partial\Theta} \vec{v}\cdot\vec{n}\, d\partial\Theta \\
&= \lim_{\Theta\to\{P_0\}} \int_0^{2\pi} \vec{v}\cdot\vec{n}(\zeta(t))\|\frac{d\zeta(t)}{dt}\|dt \\
&= \lim_{\Theta\to\{P_0\}} \int_0^{2\pi} \vec{v}\cdot\vec{n}(\zeta(t))\frac{r'}{\sqrt{1+(r')^2}}dt \\
&= \lim_{\Theta\to\{P_0\}} \frac{1}{\sqrt{1+(r')^2}} \int_0^{2\pi} \vec{v}'\cdot\vec{n}'(\zeta'(t))r'dt \\
&= \lim_{\Theta\to\{P_0\}} \frac{1}{\sqrt{1+(r')^2}} \int_0^{2\pi} \vec{v}'\cdot\vec{n}'(\zeta'(t))\|\frac{d\zeta'(t)}{dt}\|dt \\
&= \lim_{\Theta\to\{P_0\}} \frac{1}{\sqrt{1+(r')^2}} \int_{\partial\Theta'} \vec{v}'\cdot\vec{n}'\, d\partial\Theta' \\
&= \lim_{\Theta'\to\{P_0\}} \int_{\partial\Theta'} \vec{v}'\cdot\vec{n}'\, d\partial\Theta' \\
&= \mathrm{div}(\vec{v}')(P_0)
\end{aligned}$$

where we used that the vector projection preserves fluxes at boundaries, that is, $\vec{v}\cdot\vec{n}(\zeta(t)) = \vec{v}'\cdot\vec{n}'(\zeta'(t))$, and also that $\lim_{\Theta\to\{P_0\}} \frac{1}{\sqrt{1+(r')^2}} = 1$.

References

[1] C. Ronchi, R. Iacono, P. S. Paolucci, The cubed sphere: a new method for the solution of partial differential equations in spherical geometry, J. Comput. Phys. 124 (1) (1996) 93–114.

[2] R. Heikes, D. A. Randall, Numerical integration of the shallow-water equations on a twisted icosahedral grid. Part I: basic design and results of tests, Mon. Wea. Rev. 123 (6) (1995) 1862–1880.

[3] D. L. Williamson, The evolution of dynamical cores for global atmospheric models, J. Meteorol. Soc. Jpn. 85B (2007) 241–269.

[4] D. P. Bacon, N. N. Ahmad, Z. Boybeyi, T. J. Dunn, M. S. Hall, P. C. S. Lee, R. A. Sarma, M. D. Turner, K. T. Waight, S. H. Young, J. W. Zack, A dynamically adapting weather and dispersion model: the operational multiscale environment model with grid adaptivity (OMEGA), Mon. Wea. Rev. 128 (7) (2000) 2044–2076.

[5] H. Tomita, M. Tsugawa, M. Satoh, K. Goto, Shallow water model on a modified icosahedral geodesic grid by using spring dynamics, J. Comput. Phys. 174 (2) (2001) 579–613.

[6] D. Majewski, D. Liermann, P. Prohl, B. Ritter, M. Buchhold, T. Hanisch, G. Paul, W. Wergen, J. Baumgardner, The operational global icosahedral-hexagonal gridpoint model GME: description and high-resolution tests, Mon. Wea. Rev. 130 (2) (2002) 319–338.

[7] L. Bonaventura, T. Ringler, Analysis of discrete shallow-water models on geodesic delaunay grids with C-type staggering, Mon. Wea. Rev. 133 (8) (2005) 2351–2373.

[8] P. Rípodas, A. Gassmann, J. Förstner, D. Majewski, M. Giorgetta, P. Korn, L. Kornblueh, H. Wan, G. Zängl, L. Bonaventura, T. Heinze, Icosahedral shallow water model (ICOSWM): results of shallow water test cases and sensitivity to model parameters, Geosci. Model Dev. Discuss. 2 (1) (2009) 581–638.
[9] J.-W. Bao, S. Benjamin, R. Bleck, J. Brown, J. Lee, A. MacDonald, J. Middlecoff, N. Wang, FIM documentation, Tech. rep., Earth System Research Laboratory - National Oceanic and Atmospheric Administration (NOAA) (March 2011).
[10] R. L. Walko, R. Avissar, The Ocean-Land-Atmosphere Model (OLAM). Part I: shallow-water tests, Mon. Wea. Rev. 136 (11) (2008) 4033–4044.
[11] M. Satoh, T. Matsuno, H. Tomita, H. Miura, T. Nasuno, S. Iga, Nonhydrostatic icosahedral atmospheric model (NICAM) for global cloud resolving simulations, J. Comput. Phys. 227 (7) (2008) 3486–3514.
[12] A. Staniforth, J. Thuburn, Horizontal grids for global weather and climate prediction models: a review, Quart. J. R. Met. Soc. 138 (662) (2012) 1–26.
[13] H. Weller, J. Thuburn, C. J. Cotter, Computational modes and grid imprinting on five quasi-uniform spherical C-grids, Mon. Wea. Rev. 140 (8) (2012) 2734–2755.
[14] H. Tomita, M. Satoh, K. Goto, An optimization of the icosahedral grid modified by spring dynamics, J. Comput. Phys. 183 (1) (2002) 307 – 331.
[15] R. Heikes, D. A. Randall, Numerical Integration of the Shallow-Water Equations on a Twisted Icosahedral Grid. Part II. A Detailed Description of the Grid and an Analysis of Numerical Accuracy, Mon. Wea. Rev. 123 (6) (1995) 1881–1887.
[16] Q. Du, M. D. Gunzburger, L. Ju, Constrained centroidal Voronoi tessellations for surfaces, SIAM J. Sci. Comput. 24 (2003) 1488–1506.
[17] L. Ju, T. Ringler, M. Gunzburger, Voronoi tessellations and their application to climate and global modeling, in: P. Lauritzen, C. Jablonowski, M. Taylor, R. Nair, T. J. Barth, M. Griebel, D. E. Keyes, R. M. Nieminen, D. Roose, T. Schlick (Eds.), Numerical techniques for global atmospheric models, Vol. 80 of Lect. Notes Comput. Sci. Eng., Springer Berlin Heidelberg, 2011, pp. 313–342.
[18] H. Miura, M. Kimoto, A comparison of grid quality of optimized spherical hexagonal-pentagonal geodesic grids, Mon. Wea. Rev. 133 (10) (2005) 2817–2833.
[19] R. D. Nair, P. H. Lauritzen, A class of deformational flow test cases for linear transport problems on the sphere, J. Comput. Phys. 229 (23) (2010) 8868 – 8887.
[20] R. J. Renka, Algorithm 773: SSRFPACK: interpolation of scattered data on the surface of a sphere with a surface under tension, ACM Trans. Math. Softw. 23 (1997) 435–442.
[21] H. Wan, Developing and testing a hydrostatic atmospheric dynamical core on triangular grids, Ph.D. thesis, International Max Planck Research School on Earth System Modelling, Max Planck Institute for Meteorology, Hamburg, Germany (2009).